I&EC research
Industrial & Engineering Chemistry Research

Article

pubs.acs.org/IECR

Impact of Wall Heat Transport on Formation of Transversal Hot Zones in Shallow, Non-adiabatic Packed-Bed Reactors

K. Narendiran and Ganesh A. Viswanathan*

Department of Chemical Engineering, Indian Institute of Technology Bombay, Powai, Mumbai 400076, India

Supporting Information

ABSTRACT: Transversal hot zones have been reported to form in packed-bed reactors used to conduct exothermic reactions. Packed-bed reactors are usually operated under non-adiabatic conditions. Previous attempts to predict the formation of transversal hot zones have been made on both shallow and long reactors under adiabatic conditions; that is, wall heat transport is zero. We show that a rich variety of slowly oscillating transversal hot zones, such as rotating patterns, targets, and spirals, may form in shallow, non-adiabatic reactors. Under certain conditions, azimuthally symmetric target patterns coexist with azimuthally non-symmetric rotating patterns. Surprisingly, a small wall heat transport can force a traveling wave or band motion observed under adiabatic conditions into a rotating pattern. A transition from the rotating patterns and/or target patterns to spiral waves depends on the residence time, the reactor length scale, and the wall heat transfer coefficient. A shallow reactor model predicts that the spatiotemporal patterns oscillate at a very low frequency (order of 10^{-5} Hz), which is in agreement with predictions based on laboratory experiments.

INTRODUCTION

A symmetric temperature (and conversion) profile is expected in the cross-section of non-adiabatic, catalytic packed-bed reactors. However, several industrial- and laboratory-scale reactor studies have reported the formation of transversal hot zones, i.e., temperature fronts. Boreskov et al.[1] and Matros[2] observed several high-temperature zones at the exit of a down-flow packed-bed reactor during partial oxidation of isobutyl alcohol. Clinker formation—that is, formation of small lumps of molten catalyst—has been reported during hydro-desulfurization of trickle-bed reactors.[3] Periodic oscillations of transversal hot zones during catalytic oxidation of CO or ethylene have been reported by Wicke and Onken.[4,5] Spatiotemporal pattern formation has been detected using infrared imaging along the exterior surface of a radial flow reactor[6,7] and thin annular catalytic shell,[8] on top of shallow packed-bed reactors,[9−11] on a catalytic glass fiber cloth reactor,[12] and in packed-bed reactors.[13] Various experimental and theoretical studies on pattern formation in different packed-bed reactor configurations, using different kinetic rate expressions, have been extensively reviewed by Viswanathan et al.[14]

Hot zone formation may strongly affect the yield of desired product(s), deactivate the catalyst, and/or trigger unwanted side reactions. The presence of hot spots, especially near the reactor wall, can pose severe safety concerns, as the high-temperature zone can weaken the metal strength, leading to formation of cracks through which the reactants and products may leak out and trigger explosions. Several explosions in trickle-bed reactors are thought to have been triggered by hot zones present near the reactor wall. Due to the lack of an appropriate non-invasive, *in situ* technique, detection of small transversal hot regions in large commercial reactors is very difficult. Therefore, understanding the formation and evolution of hot zones in packed-bed reactors can provide useful insights for identification of potential strategies for circumventing their formation, especially near reactor walls. Potential causes for local hot spot formation in catalytic packed-bed reactors that have been considered in the literature include non-uniform catalyst activity/packing,[2,15] flow maldistribution,[16,17] hydrodynamic instabilities,[18,19] or global coupling due to interaction of (a) unreacted reactants in the effluent stream with the top of the packed-bed reactor[20] and (b) reactants with the surface of the annular cylinder.[8,21] Pattern formation due to spatial non-uniform catalytic activity may be caused by point contact between discrete catalyst particles in the solid phase.[15]

Symmetry-breaking bifurcation leading to formation of spatial and/or spatiotemporal patterns is a ubiquitous phenomenon. Several attempts have been made to predict and understand pattern formation in adiabatic packed-bed reactors caused by symmetry-breaking. Schmitz and Tsotsis[22] found that stationary hot zones may form when the rate of species exchange exceeds that of the heat exchange. Balakotaiah et al.[23] showed that, in an adiabatic reactor used to conduct a bimolecular reaction, transversal patterns may form when the heat dispersion is lower than that of the species. However, as pointed out by Yakhnin and Menzinger,[24] under practical conditions, heat dispersion is higher than that of the species in packed-bed reactors.[25,26] Neither a pseudo-homogeneous model[27] nor a two-phase model[28] accounting for only temperature and concentration variables can predict the formation of stable, symmetry-breaking, stationary transversal patterns when the heat dispersion is higher than that of the species. A detailed rate expression that considers, in addition to temperature and reactant concentration, dynamics of the

Received: March 19, 2015
Revised: June 10, 2015
Accepted: July 8, 2015

DOI: 10.1021/acs.iecr.5b01048
Ind. Eng. Chem. Res. XXXX, XXX, XXX−XXX

adsorbed concentration of non-limiting reactant or catalytic activity may permit formation of a rich variety of spatiotemporal patterns, such as rotating patterns and complex periodic motion in two and three dimensions (2-D and 3-D). This has been demonstrated for shallow[29,30] and (more realistic) long adiabatic reactors.[31,32] Such rate expressions that depend on the adsorbed concentration of non-limiting reactant or local catalytic activity and permit oscillations have been validated for several exothermic reactions, such as CO oxidation,[33] ethylene hydrogenation,[33] and oxidation of hydrogen.[34]

Significant attempts have been made to predict spatial and spatiotemporal pattern formation in adiabatic packed-bed reactors. However, achieving perfect adiabatic conditions is extremely difficult. In fact, most industrial reactors used for conducting exothermic reactions are cooled[35] for better heat management. Laboratory-scale reactors typically use alumina wool to minimize heat loss from the walls.[9] Thus, it is necessary to obtain insights on the pattern formation in non-adiabatic reactors as well. In this study, we consider the formation of spatiotemporal patterns in non-adiabatic, catalytic packed-bed reactors. Nekhamkina and Sheintuch[36] showed that, for a homogeneous model with first-order exothermic kinetics, under non-adiabatic conditions, at best only axisymmetric patterns such as targets can be obtained. Using a periodic blocking−reactivation kinetic model, we predict formation of a rich variety of spatiotemporal patterns, such as rotating patterns and spirals, in shallow, non-adiabatic packed-bed reactors.

CALCULATIONS AND MODELING

Shallow, Non-adiabatic Packed-Bed Reactor Model. We consider transversal hot zone formation during the ethylene hydrogenation reaction,

$$C_2H_4 + H_2 \rightarrow C_2H_6 \tag{1}$$

conducted in a catalytic packed-bed reactor filled with Pd-impregnated catalysts and operated under non-adiabatic conditions. We model this system by monitoring the blocking of catalyst sites, local reactor temperature, and concentration. First, assuming a periodic blocking−reactivation of Pd catalyst sites,[30,33,37] the dynamics of the fractional active-site blocking is captured by

$$\frac{d\Theta}{d\tau} = Da_{BL}\mathbb{B}_1(\theta, \Theta) - Da_{RE}\mathbb{B}_2(\theta, \Theta) \tag{2}$$

where θ (= $(T - T_{in})/T_{in}$) and Θ respectively are the local dimensionless temperature and fraction of blocked catalytically active sites,

$$\mathbb{B}_1(\theta, \Theta) = \exp\left[\frac{\gamma_{BL}\theta}{1+\theta}\right](1-\Theta), \qquad \mathbb{B}_2(\theta, \Theta) = \exp\left[\frac{\gamma_{RE}\theta}{1+\theta}\right]\Theta \tag{3}$$

and

$$\tau = \frac{vt}{L}, \quad \gamma_{BL} = \frac{E_{BL}}{\bar{R}T_{in}}, \quad \gamma_{RE} = \frac{E_{RE}}{\bar{R}T_{in}}, \quad Da_{BL} = \frac{L}{v}k_{BL}(T_{in}), \quad Da_{RE} = \frac{L}{v}k_{RE}(T_{in}) \tag{4}$$

with $k_{BL}(T_{in}) = k^0_{BL}\ e^{-\gamma_{BL}}$ and $k_{RE}(T_{in}) = k^0_{RE}\ e^{-\gamma_{RE}}$. Next, we capture the dynamics of the conversion x (= $1 - C/C_{in}$) and temperature θ in the non-adiabatic reactor using a pseudo-homogeneous model. Dimensionless model equations for these quantities are

$$\frac{\partial x}{\partial \tau} + \frac{\partial x}{\partial \eta} - \frac{1}{Pe_a^m}\frac{\partial^2 x}{\partial \eta^2} - \frac{1}{Pe_\perp^m}\nabla_\perp^2 x - \mathbb{R}(x, \theta, \Theta) = 0 \tag{5}$$

$$Le\frac{\partial \theta}{\partial \tau} + \frac{\partial \theta}{\partial \eta} - \frac{1}{Pe_a^h}\frac{\partial^2 \theta}{\partial \eta^2} - \frac{1}{Pe_\perp^h}\nabla_\perp^2\theta - \beta\mathbb{R}(x, \theta, \Theta) = 0 \tag{6}$$

subject to the boundary conditions

$$\frac{\partial x}{\partial \eta} = Pe_a^m x, \quad \frac{\partial \theta}{\partial \eta} = Pe_a^h\theta \quad @ \quad \eta = 0; \qquad \frac{\partial x}{\partial \eta} = \frac{\partial \theta}{\partial \eta} = 0 \quad @ \quad \eta = 1 \tag{7a}$$

$$\frac{\partial x}{\partial \xi} = 0, \quad \frac{\partial \theta}{\partial \xi} = -Bi(\theta - \theta_w) \quad @ \quad \xi = 1 \tag{7b}$$

where the dimensionless quantities are

$$\theta_w = \frac{T_w}{T_{in}} - 1, \quad \eta = \frac{z}{L}, \quad \xi = \frac{r}{R}, \quad \gamma = \frac{E}{\bar{R}T_{in}}, \quad Pe_a^h = \frac{vL}{\bar{\lambda}_a/(\rho C_p)_f}, \quad Pe_a^m = \frac{vL}{D_a}, \quad Pe_\perp^h = \frac{vR^2}{L\bar{\lambda}_\perp/(\rho C_p)_f}, \quad Pe_\perp^m = \frac{vR^2}{LD_\perp}, \quad Bi = \frac{hR}{\bar{\lambda}_\perp}, \quad \beta = \frac{(-\Delta H)C_{in}}{(\rho C_p)_f T_{in}}, \quad Le = \varepsilon + (1-\varepsilon)\frac{(\rho C_p)_s}{(\rho C_p)_f}, \quad k(T_{in}) = k^0 e^{-\gamma}, \quad Da = \frac{L}{v}k(T_{in}) \tag{8}$$

with subscript $\perp$ referring to the transversal direction (perpendicular to the flow). In eqs 5 and 6, $\nabla_\perp^2$ is the Laplacian operator in polar coordinates:

$$\nabla_\perp^2 = \left[\frac{1}{\xi}\frac{\partial}{\partial \xi}\left(\xi\frac{\partial}{\partial \xi}\right) + \frac{1}{\xi^2}\frac{\partial^2}{\partial \phi^2}\right]$$

Assuming ethylene is present in excess, the dimensionless reaction rate that is first-order with respect to hydrogen is given by

$$\mathbb{R}(x, \theta, \Theta) = Da\ \exp\left[\frac{\gamma\theta}{1+\theta}\right](1-x)(1-\Theta) \tag{9}$$

Identification of the spatiotemporal patterns permitted by the model requires the use of appropriate 3-D initial conditions, which is very difficult and tedious to arrive at.[27,29] Therefore, to gain useful insights into the formation and dynamics of hot zones, we first study the shallow reactor model under non-adiabatic conditions, which is a limiting form of the full model[14] and can be obtained using the Liapunov−Schmidt reduction of the full model (eqs 2−9).[38,39] [Details of the method have been described by Viswanathan.[40]] This approach has been demonstrated successfully for models of reactor operated under adiabatic conditions.[27−29,41] We extend this to non-adiabatic reactor model. The pseudo-homogeneous model of the shallow, non-adiabatic packed-bed reactor (SNAR) is

DOI: 10.1021/acs.iecr.5b01048
Ind. Eng. Chem. Res. XXXX, XXX, XXX−XXX

$$\frac{\partial x}{\partial \tau} = -x + \frac{1}{Pe_{\perp}^{m}}\left[\frac{1}{\xi}\frac{\partial}{\partial \xi}\left(\xi\frac{\partial x}{\partial \xi}\right) + \frac{1}{\xi^2}\frac{\partial^2 x}{\partial \phi^2}\right] + \mathbb{R}(x, \theta, \Theta) \tag{10}$$

$$Le\frac{\partial \theta}{\partial \tau} = -\theta + \frac{1}{Pe_{\perp}^{h}}\left[\frac{1}{\xi}\frac{\partial}{\partial \xi}\left(\xi\frac{\partial \theta}{\partial \xi}\right) + \frac{1}{\xi^2}\frac{\partial^2 \theta}{\partial \phi^2}\right] + \beta\mathbb{R}(x, \theta, \Theta) \tag{11}$$

where the axially averaged dimensionless conversion and temperature are

$$x = \int_0^1 x\ d\eta \qquad \theta = \int_0^1 \theta\ d\eta \tag{12}$$

with the corresponding boundary conditions being

$$\frac{\partial x}{\partial \xi} = 0 \quad @ \quad \xi = 1 \tag{13a}$$

$$\frac{\partial \theta}{\partial \xi} = -Bi(\theta - \theta_w) \quad @ \quad \xi = 1 \tag{13b}$$

The dynamics of Θ is captured by eq 2. Using $L = d_p$,[27] where d_p is the particle diameter, we redefine transversal mass and heat Peclet numbers respectively as $Pe_{\perp}^{m} = Pe_p^{m}(R/d_p)^2$, with $Pe_p^{m} = vd_p/D_{\perp}$, and $Pe_{\perp}^{h} = Pe_p^{h}(R/d_p)^2$, with $Pe_p^{h} = vd_p/(\bar{\lambda}_{\perp}/(\rho C_p)_f)$. Biot number is rewritten as $Bi = Bi_p(R/d_p)$, with $Bi_p = hd_p/\bar{\lambda}_{\perp}$.

Using second-order finite difference scheme, the SNAR model (eqs 2, 10, 11 and 13) was discretized in polar coordinates. The reactor was divided into N circles placed at $\xi_i = ((2i - 1)/(2N - 1))\forall i = 1, N$.[31,42] Each circle consisted of equally spaced grids in azimuthal direction. This discretization scheme circumvents numerical difficulties associated with the singularity at the center ($\xi = 0$). Dynamic simulations were performed using Linear IMplicit Extrapolator (LIMEX).[43,44] While simulations of the azimuthally uniform state were conducted using direct linear solver (LAPACK) option in LIMEX, the 2-D simulations were performed using the underlying sparse iterative solver (BiGSTAB), which usually converged in 3−4 iterations. All steady-state simulations were conducted using Newton−Raphson iteration implemented in Nonlinear Object-Oriented Solutions (NOX) package in Trilinos.[45] Bifurcation diagrams and maps were constructed using pseudo-arc length continuation technique available in Library of Continuation Algorithms (LOCA)[46] in Trilinos.[45]

Methodology for Predicting Spatiotemporal Patterns. A non-adiabatic shallow reactor can permit spatiotemporal transversal patterns whose dynamics may depend solely on the radial position or on both radial and azimuthal coordinates. The procedure that has been followed for the case of adiabatic reactor is *not* directly amenable for non-adiabatic conditions. This is due to the fact that, under non-adiabatic conditions, the flux boundary condition forces a symmetric base steady state, $\boldsymbol{u}_{ss} = \boldsymbol{u}_{ss}(\xi) = [x_{ss}(\xi)\ \theta_{ss}(\xi)\ \Theta_{ss}(\xi)]^t$, in the transversal direction, that is, a function of radial position. The base state $\boldsymbol{u}_{ss}$ is the solution of the 1-D steady-state SNAR model obtained by ignoring the time and azimuthal dependence in eqs 2, 10, 11 and 13. [Note that under adiabatic conditions, the base steady state is transversally uniform.] As the nature of the base steady state is different under non-adiabatic conditions, the overall procedure prescribed for adiabatic conditions elsewhere[29] needs to be modified based on the extent to which pattern of interest depends on the physical dimensions. We briefly sketch the overall procedure followed for obtaining patterned states under non-adiabatic conditions.

The stationary steady state $\boldsymbol{u}_{ss}$ is stable to homogeneous perturbations $\boldsymbol{\omega}(\xi) = [\omega_1(\xi)\ \omega_2(\xi)\ \omega_3(\xi)]^t$ when all eigenvalues of the underlying eigenvalue problem,

$$\mathbb{D}_{\boldsymbol{u}}\mathbb{F}|_{\boldsymbol{u}_{ss}}\cdot\boldsymbol{\omega} = \begin{bmatrix} 1 - \frac{\nabla_{\perp,r}^2}{Pe_{\perp}^{m}} - \mathbb{R}_x & -\mathbb{R}_\theta & -\mathbb{R}_\Theta \\ -\frac{\beta}{Le}\mathbb{R}_x & \frac{1}{Le}\left\{1 - \frac{\nabla_{\perp,r}^2}{Pe_{\perp}^{h}} - \beta\mathbb{R}_\theta\right\} & -\frac{\beta}{Le}\mathbb{R}_\Theta \\ 0 & Da_{BL}\mathbb{B}_{1\theta} - Da_{RE}\mathbb{B}_{2\theta} & Da_{BL}\mathbb{B}_{1\Theta} - Da_{RE}\mathbb{B}_{2\Theta} \end{bmatrix}_{\boldsymbol{u}_{ss}}\cdot\boldsymbol{\omega} = \lambda\boldsymbol{\omega} \tag{14}$$

subject to the boundary conditions $\partial\omega_1/\partial\xi|_{\xi=1} = 0$ and $(\partial\omega_2/\partial\xi + Bi\omega_2)_{\xi=1} = 0$, have negative real part. The eigenvalue problem (eq 14) is obtained by introducing the perturbations $\boldsymbol{u} - \boldsymbol{u}_{ss} = \boldsymbol{\omega}\exp(\lambda\tau)$, where the state variables $\boldsymbol{u} = [x(\xi)\ \theta(\xi)\ \Theta(\xi)]^t$, into the 1-D SNAR model and linearizing around the base steady state $\boldsymbol{u}_{ss}$. In eq 14, $\mathbb{F}$ is the vector of 1-D steady-state model equations, $\mathbb{D}_{\boldsymbol{u}}\mathbb{F}|_{\boldsymbol{u}_{ss}}$ is the first Fréchet derivative of $\mathbb{F}$ evaluated at $\boldsymbol{u}_{ss}$, and $\mathbb{R}_x$, $\mathbb{R}_\theta$, and $\mathbb{R}_\Theta$ respectively are the partial derivatives of the dimensionless reaction rate $\mathbb{R}(\boldsymbol{u})$ with respect to the state variables x, θ, and Θ. While $\mathbb{B}_{1\theta}$, $\mathbb{B}_{1\Theta}$, and $\mathbb{B}_{2\theta}$, and $\mathbb{B}_{2\Theta}$ respectively are the partial derivatives of the dimensionless blocking and reactivation rates with respect to θ and Θ, $\nabla_{\perp,r}^2$ is the Laplacian in radial coordinates. [In eq 14, · refers to dot product.] Note that due to the *a priori* unknown dependence of the derivatives $\mathbb{R}_x$, $\mathbb{R}_\theta$, and $\mathbb{R}_\Theta$ (evaluated at $\boldsymbol{u}_{ss}$) on ξ, and therefore that of $\mathbb{B}_{1\theta}$, $\mathbb{B}_{1\Theta}$, $\mathbb{B}_{2\theta}$, and $\mathbb{B}_{2\Theta}$ also implicitly on ξ, the eigenvalue problem in eq 14 along with the boundary conditions, though linear, cannot be solved analytically. While a limit point bifurcation occurs when a real eigenvalue of $\mathbb{D}_{\boldsymbol{u}}\mathbb{F}|_{\boldsymbol{u}_{ss}}$ is zero, a Hopf bifurcation occurs when a pair of complex eigenvalues of $\mathbb{D}_{\boldsymbol{u}}\mathbb{F}|_{\boldsymbol{u}_{ss}}$ crosses the imaginary axis with non-zero speed. The periodic blocking-reactivation kinetic model considered here permits stable, purely radial oscillatory behavior (presented later).

Parameter ranges where 2-D transversal spatiotemporal patterns may appear were identified by finding the boundaries in parameter space where the stable azimuthally homogeneous states may become unstable. A stable azimuthally homogeneous state $\boldsymbol{u}_{ss}$ may become unstable when subject to azimuthally inhomogeneous perturbations of the form

$$\boldsymbol{\omega}_m(\xi, \phi) = \boldsymbol{\omega}(\xi)e^{im\phi} \tag{15}$$

where $m = 1, 2, 3, \ldots$ is the azimuthal mode number and $e^{im\phi}$ is the m^{th} eigenfunction. This transition occurs at the Hopf neutral stability point which satisfies

$$\mathbb{F}(\boldsymbol{u}_{ss}, Da) = 0 \tag{16}$$

$$[\mathbb{D}_{\boldsymbol{u}}\mathbb{F}|_{\boldsymbol{u}_{ss}} - \mathbb{P}]\cdot(\boldsymbol{\omega}_r(\xi) \pm i\boldsymbol{\omega}_i(\xi)) = \pm i\sigma(\boldsymbol{\omega}_r(\xi) \pm i\boldsymbol{\omega}_i(\xi)) \tag{17}$$

where $\mathbb{P}$ is the azimuthal perturbation matrix,

$$\mathbb{P} = \begin{bmatrix} m^2 & 0 & 0 \\ 0 & m^2 & 0 \\ 0 & 0 & 0 \end{bmatrix}$$

DOI: 10.1021/acs.iecr.5b01048
Ind. Eng. Chem. Res. XXXX, XXX, XXX−XXX

and $\boldsymbol{\omega}_r$ and $\boldsymbol{\omega}_i$ respectively are the real and imaginary parts of the complex eigenvector $\boldsymbol{\omega}(\xi)$, corresponding to the complex eigenpair $\lambda = \pm i\sigma$, with σ being the frequency (up to first-order terms) of the emerging oscillations. Details of the construction of the Hopf neutral stability locus are in Appendix I-1.

In order to find a specific sustained spatiotemporal pattern, we provide an inhomogeneous initial guess to the 2-D model equations (eqs 2, 10, 11, and 13),

$$\boldsymbol{u}(\xi, \phi) = \boldsymbol{u}_{ss}(\xi) + A_c \boldsymbol{\omega}(\xi) e^{im\phi} \tag{18}$$

with the specific value of m and $A_c \approx 0.5$, and solve for the trajectories of the state variables for sufficient number of stable cycles using the procedure outlined in the previous section.

Note that the purely radial or azimuthally uniform spatiotemporal patterns are a subset of the various possible spatiotemporal patterns. It has been noted by Golubitsky et al.[47] that the purely radial spatiotemporal patterns are obtained when $m = 0$. For the model considered here, these states are the azimuthally homogeneous 1-D oscillations or *symmetric targets* obtained by using base states itself as initial conditions.

In the following sections, we use the procedure outlined here to predict various spatiotemporal patterns. Parameter values used in all simulations, unless otherwise mentioned, are

$$\gamma = 15, \quad \gamma_{BL} = 7.7, \quad \gamma_{RE} = 0.77, \quad Da_{BL} = 3e-5,$$
$$Da_{RE} = 1e-5, \quad Pe_p^m = 5, \quad Pe_p^h = 1,$$
$$Le = 1416, \quad \beta = 0.95, \quad \theta_w = 0.9 \tag{19}$$

Spatiotemporal Pattern Formation. Evolution of different types of spatiotemporal patterns is a strong function of the base-state solution from which the patterned state emerges and the initial conditions that are provided to the dynamic simulations. The base-state solution, under certain conditions, exhibits multiple steady states and oscillatory behavior. The bifurcation map in the planes of Da and Bi_p (Figure 1a) shows, for $R/d_p = 100$, via the codimension-1 (henceforth codim-1) limit point (gray lines in Figure 1a) and (supercritical) Hopf bifurcation (black lines in Figure 1a) loci, the parameter region where the multiple steady states and the oscillatory dynamical behavior exist. [Details of the construction of the codim-1 limit point locus are in Appendix I-2.] For the chosen set of parameters (eq 19), the oscillatory states (Figure 1a, black lines) and the limit points (Figure 1a, inset) were found even when $Bi_p = 0$, that is, adiabatic conditions, as reported in previous studies.[30] For a fixed wall temperature, θ_w, as the rate of heat transport from the reactor wall depends both on wall heat transfer coefficient (Bi_p) and on the reactor radius (R/d_p), modulation of the Hopf bifurcation by the reactor radius is important and is captured via the codim-1 Hopf locus (dotted lines) in Figure 1b. Note that (a) the oscillatory states, if any, are bounded between two supercritical Hopf bifurcation points, and (b) for a sufficiently large Bi_p (Figure 1a) and sufficiently large reactor radius (Figure 1a,b), the Hopf bifurcation is not modulated by either wall heat transfer coefficient or the reactor radius. We next present, in Figure 1b, along with the Hopf codim-1 locus, the oscillatory neutral stability curves for the first three azimuthal modes ($m = 1, 2, 3$). Oscillatory neutral stability curve for a particular m is the locus of those marginal stability points from where the transversal patterns may emerge from the bases states. [Note that while a very large number of transversal patterns may be generated using initial conditions with different values of m, we restrict to the first three modes only in this study.] The contours of the eigenfunction of the underlying perturbations $(\boldsymbol{\omega}(\xi)e^{im\phi}$ in eq 18) for $Da = 0.195$ are depicted in Figure 1c. Contours for others values of Da are similar. Extensive numerical simulations were performed for various parameter values using inhomogeneous initial conditions as shown in eq 18 for various m. Numerical simulations showed the existence of a rich variety of patterns and the transitions between them.

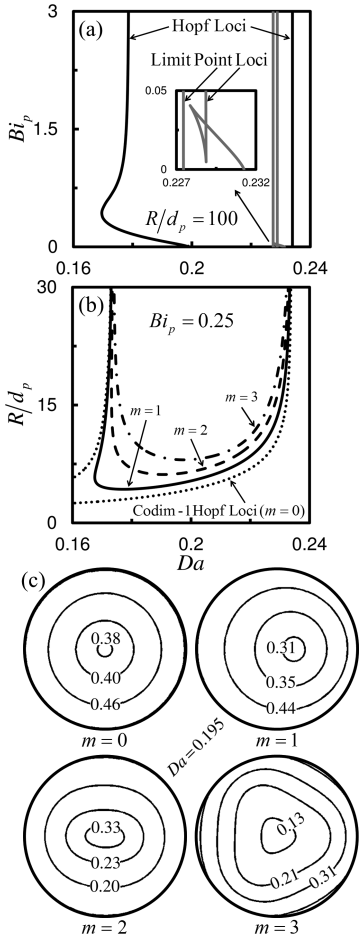

Figure 1. (a) Codimension-1 bifurcation map showing the Hopf-bifurcation and limit point loci for $R/d_p = 100$. Inset: Zoom-in on a section of the limit point locus. (b) Hopf bifurcation locus (corresponding to $m = 0$) and the oscillatory neutral stability curves for the first three azimuthal modes ($m = 1, 2, 3$) for $Bi_p = 0.25$. (c) Level contours of transversal eigenmodes for $m = 0, 1, 2, 3$ at $Da = 0.195$ on the loci in (b).

We first show the case of a reactor with relatively small $R/d_p = 10$. In Figure 2, we present the global bifurcation diagram in the planes of Da (representing residence time) and the exit temperature $\langle\theta\rangle$, which is obtained by taking a cross-sectional average of the temperature. Two supercritical Hopf bifurcations (H_1 and H_2 in Figure 2) emerge from the stable base steady states (solid black) with the imaginary coefficient of the eigenvalue, that is, frequency σ being 0.000177 and 0.000213, respectively. Thus, the period of oscillations next to the two Hopf points H_1 and H_2 of $2\pi/\sigma$ is 35498 and 29499, respectively. While both target and rotating patterns emerge from H_1, only target patterns emerge from H_2. The dependence of the rotating (solid gray) and target (dotted) patterns on the Da are captured by monitoring the maximal $\langle\theta\rangle$ during one cycle of the oscillation. [Note that the rotating patterns were

DOI: 10.1021/acs.iecr.5b01048
Ind. Eng. Chem. Res. XXXX, XXX, XXX−XXX

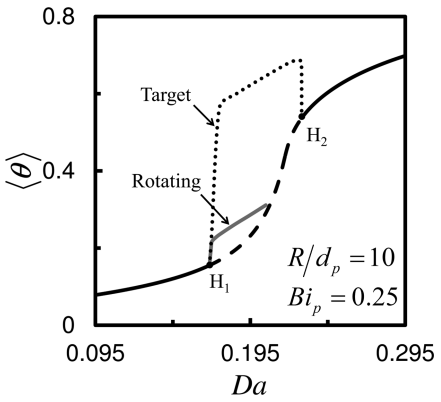

Figure 2. Global bifurcation diagram showing the dependence of the exit temperature $\langle\theta\rangle$ on *Da* for the 1-D base steady states (solid black, stable; dashed black, unstable), rotating (solid gray) patterns, and target (dotted) patterns. H_1 and H_2 are the Hopf bifurcation points.

obtained by providing an initial guess with $m = 1$ in eq 18. For the parameters considered, extensive simulations suggested that use of eigenfunctions corresponding to $m = 2,3$ as initial conditions typically led to formation of target patterns. Thus, in all the cases reported here, we used as initial conditions only those based on $m = 1$.] Rotating and target patterns coexisted for *Da* from ~0.17 to ~0.205. Dynamic simulations suggested that beyond *Da* = 0.205, until H_2, the initial guess corresponding to $m = 1$ led to target patterns only.

The dynamics of the exit temperature $\langle\theta\rangle$ of rotating patterns and targets at *Da* = 0.195 are presented in Figure 3a,d, respectively. [Note that the dimensionless time τ in abscissa is scaled with *Le*.] The amplitude of oscillation $\mathcal{A}_p$ exhibited by exit temperature for the case of rotating patterns is about 2 orders of magnitude smaller than that of targets. However, period of oscillation (P) is similar for both patterns, that is, 23.66 and 26.48 (in τ/Le units) for the rotating and target patterns, respectively.

Spatial profiles of the rotating patterns in one cycle at τ/Le = 0, $P/4$, $P/2$, $3P/4$, and P are shown in Figure 3b. During a cycle, at $\tau/Le = 0$, the hot zone is formed in the right half of the cross-section. As time progresses, the front separating the hot and cold regions at the 4 o'clock position is propelled forward, making the hot zone rotate in the clockwise direction; the receding front of the hot zone also moves in the clockwise direction. A rational method to characterize the rotating patterns is to monitor the tip motion. A method for identifying and tracking of the tip of a rotating pattern has been proposed for a two-variable problem.[32] In this study, we extend this to a three-variable problem by observing that the spatiotemporal dynamics of the average temperature and average conversion variables are in sync with each other, while the average activity is not (see Figure S1 in Supporting Information). [We also found that the spatial 2-D gradients of the activity variable drive the temperature and conversion (data not shown).] This observation suggests that local temperature, which is considered an activator in packed-bed reactors,[31] introduces a frame-invariant rotation to the activity, and in turn, activity introduces a frame-invariant rotation in the temperature and conversion variables. Therefore, the tip of the rotating pattern in every frame can be identified using the condition

$$(\nabla\theta \times \nabla\Theta)_{(\xi_{tip},\phi_{tip})} = \sup\{(\nabla\theta \times \nabla\Theta)_{(\xi,\phi)} \ \forall\ (\xi, \phi)\} \tag{20}$$

where $\nabla\theta$ and $\nabla\Theta$ are the 2-D vectors representing respectively the spatial gradients of θ and Θ. In eq 20, while sup represents supremum, (ξ_{tip},ϕ_{tip}) is the location of the tip position in that frame. Rotating pattern tip follows a constant diameter circular path in the cross-section and is represented as yellow circle around the center in each of the snapshots in Figure 3b. [Henceforth, wherever pattern contains a single tip, eq 20 is used to identify the tip location.] Moreover, the path traversed by the tip from the start of the cycle up to that specific time is presented in black on the yellow tip-circle in each of the snapshots in Figure 3b. [Note that the tip position in the

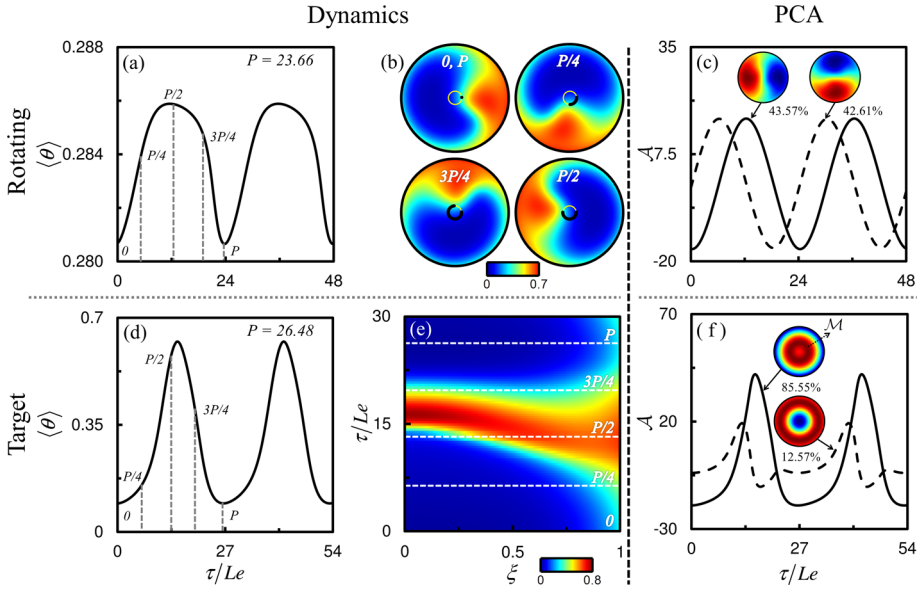

Figure 3. Time series of exit temperature $\langle\theta\rangle$ at *Da* = 0.195 for (a) rotating and (d) target patterns. P is in τ/Le units. (b) Snapshots of rotating pattern at τ/Le = 0, $P/4$, $P/2$, $3P/4$, and P. (e) Spatiotemporal dynamics of target pattern for one period. (c,f) Amplitudes of the first two PCA modes along with corresponding contours and the energy captured for the motions presented in (a,d). R/d_p = 10, Bi_p = 0.25.

DOI: 10.1021/acs.iecr.5b01048
Ind. Eng. Chem. Res. XXXX, XXX, XXX−XXX

conversion variable can be identified by replacing θ with x in eq 20.]

In Figure 3e, we present the spatiotemporal motion exhibited by the target patterns (for one cycle) showing the existence of hot (H) and cold (C) rings emerging and capturing the whole cross-section. In a cycle, first, the hot ring (target) emerges at the wall ($\xi = 1$), and the front moves toward the center ($\xi = 0$). For $\tau/Le \approx P/2$, the ring covers the whole cross-section with maximum temperature at $\xi = 0$. The reactor maintains a high temperature for some time until the reactants are no more available. In the meantime, at $\xi = 0$, the activity goes down significantly due to product inhibition, and a cold spot is triggered. This cold wave generated at $\tau/Le \approx 3P/4$ travels toward the wall and captures the entire cross-section before the end of the cycle.

Identification of the characteristics of a spatiotemporal motion simply by inspection is difficult and tedious. Characterization of the motion can be achieved by the use of principal component analyses (PCA), which separates the motion into a combination of time-dependent orthogonal amplitudes and distinct, time-independent spatial components.[48] This separation facilitates an objective approach for extracting coherent structures embedded in the spatiotemporal data. PCA has been employed successfully to analyze spatiotemporal motion in many experimental and theoretical studies,[49] including that of packed-bed reactors.[30,31,50] The spatiotemporal data $\boldsymbol{u}(\xi,\phi,\tau)$ is expressed as a series summation of the form

$$\boldsymbol{u}(\xi, \phi, \tau) = \sum_{i=1}^{n} \mathcal{A}_i(\tau)\mathrm{M}_i(\xi, \phi) \tag{21}$$

where $\mathcal{A}_i(\tau)$ and $\mathrm{M}_i(\xi,\phi)$ respectively represent the orthogonal time-dependent PCA amplitudes and time-independent spatial modes or PCA modes. Details of the procedure for PCA are presented in Appendix II.

PCA of the rotating and target patterns in Figure 3a,b and d,e revealed that the first two PCA modes are sufficient to capture the maximum energy contained in the spatiotemporal dynamics. $\mathcal{A}_i(\tau)$ of the first two PCA modes and their corresponding $\mathrm{M}_i(\xi,\phi)$ for the rotating and target patterns, respectively, are presented in Figure 3c,f. The spatial profile of the first two PCA modes of rotating patterns (Figure 3c) have almost equal energy (~43%), suggesting their equal contribution to the dynamics and a $\pi/2$ rotation relative to each other. Both PCA modes are similar to those obtained for band motion or traveling waves under adiabatic conditions,[30,31] that is, when $Bi_p = 0$. On the other hand, for the case of targets, there is clearly one dominant PCA mode (with ~85% energy) contributing to the overall dynamics. Moreover, the dominant PCA mode has a maximal temperature zone ($\mathcal{M}$ in the PCA mode in Figure 3f) interspersed between two relatively colder zones.

Effect of Pattern Formation on Wall Heat Transport. Industrial-scale reactors are typically operated under non-adiabatic conditions, and poor temperature control has been reported to be one of the key causes of explosions and runaway. The temperature control of a catalytic reactor is achieved via heat exchange between the reactor and the circulating coolant. Hot zones that may form in the reactor will strongly be influenced by the wall heat transport. On the other hand, pattern formation studies on laboratory-scale reactors under adiabatic conditions have been attempted. Adiabatic conditions are typically created by thermal insulation, which are *not* perfect heat shields. In this section, we consider the effect of the wall heat transport on the dynamics of the spatiotemporal transversal patterns in the reactor and show that even a slight heat exchange causing marginal non-adiabatic conditions can have a very strong impact on the pattern formation.

The wall heat flux (rhs of eq 13b) is a function of the reactor radius (R/d_p), heat transfer coefficient (Bi_p), and wall temperature (θ_w). We conducted all simulations and analyses for a fixed wall temperature (θ_w). Here, we first consider the effect of the reactor radius on hot zone formation and dynamics. It is important to note that R/d_p, an inherent reactor length scale directly influences both the overall transversal heat and mass transport and the wall heat flux. In Figure 4a, for Bi_p = 0.25 and Da = 0.195, we present the global bifurcation diagram in the planes of R/d_p and $\langle\theta\rangle$, showing coexistence of rotating and target patterns and a threshold R/d_p above which *only* targets exist. [Note that while the target pattern branches emerge from the Hopf bifurcation (H in Figure 4a) leading to exchange of stability, rotating pattern emerges from the point where the base state solution loses stability to first azimuthal mode (m = 1) inhomogeneous perturbations. The unstable base steady state (dashed black in Figure 4a) does not gain stability due to another Hopf bifurcation even for a very large R/d_p, as is evident from Figure 1b.] Rotating patterns for R/d_p = 10, 20, and 28 along with the locus of the tip (yellow circle)

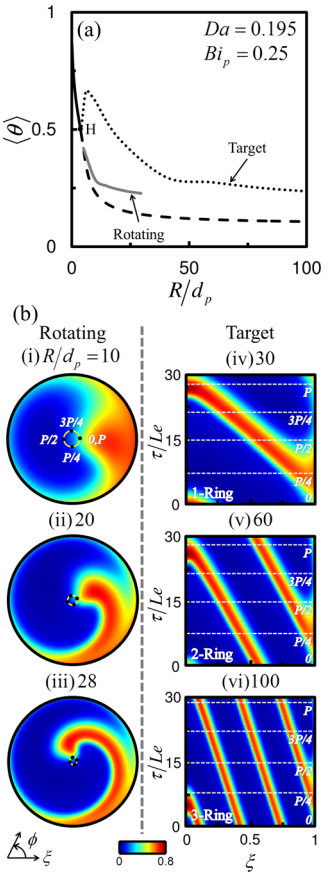

Figure 4. (a) Global bifurcation diagram showing the dependence of exit temperature $\langle\theta\rangle$ on R/d_p for 1-D base steady states (solid black, stable; dashed black, unstable), rotating (solid gray), and target (dotted) patterns. H indicates Hopf bifurcation point. (b) Snapshots of transversal temperature depicting rotating (i–iii) and target (iv–vi) patterns for different R/d_p.

DOI: 10.1021/acs.iecr.5b01048
Ind. Eng. Chem. Res. XXXX, XXX, XXX−XXX

and tip position at different fractions of P (black dots) are respectively shown in Figure 4b-i–iii. Note that while target patterns coexist for these values of R/d_p, we did not find any rotating patterns for the chosen set of parameters with $R/d_p >$ ~28. Dynamics of target patterns for R/d_p = 30, 60, and 100 respectively are presented in Figure 4b-iv–vi. Amplitude $\mathcal{A}_p$ and period of oscillation P for both rotating and target patterns for different reactor radius are given in Table 1. While the

Table 1. Amplitude $\mathcal{A}_p$ and Period of Oscillation P for Different R/d_p for the Rotating and Target Patterns in Figure 4[a]

	R/d_p					
	10	20	28	30	60	100
	Rotating Pattern					
$\mathcal{A}_p$	0.0052	0.0046	0.0031			
P	23.66	27.93	28.52			
	Target Pattern					
$\mathcal{A}_p$	0.5286	0.3880	0.2709	0.2411	0.1188	0.0640
P	26.48	28.25	28.25	28.25	29.33	29.68

[a] Da = 0.195, Bi_p = 0.25, and all other parameters as in eq 19.

period of oscillations of the rotating and target patterns, in the region where they coexisted, are comparable, the amplitudes of target patterns are 2 orders of magnitude larger than that of rotating patterns.

Increasing R/d_p from 10 to 20 increases the wall heat transport from the reactor wall. Larger reactor radius will have larger cross-sectional area for reaction. [Note that Da is kept constant; that is, the net amount of reactants available is unaltered.] As a consequence, heat generated near the outer rim would be removed relatively faster for higher R/d_p, resulting in trapping the hot zone, where the reaction occurs, inside the reactor. Moreover, the physical distance between the forward moving front and that receding shrinks as the reactor diameter is increased. Given the rotational motion already set by the temperature variable, the pattern therefore curls around (Figure 4b-ii), and the tip makes a much smaller circle (yellow). Further increase in R/d_p to 28 leads to a further increase in the wall heat transport, thereby resulting in deeper curling of the pattern, with the tip making an even smaller circle (Figure 4b-iii). However, further increase in the reactor radius to 30 makes the pattern snap-off from the reactor wall to form a ring and, thereby, transition into target patterns with one ring moving from the reactor wall to the center (Figure 4b-iv). On increasing R/d_p even further, multiple rings are formed (Figure 4b-v,vi), with two rings at R/d_p = 60 and three at R/d_p = 100. [Note that though we present the patterns for specific R/d_p, the qualitative nature of the pattern, that is, number of rings in the case of target patterns, is preserved for intermediate R/d_p.] Comparison of the leading PCA modes of the rotating and target patterns at various R/d_p corroborates the fact that increase in reactor radius can lead to onset of target patterns from rotating patterns (see Figure S2 in Supporting Information). While rotating patterns are dominated by two-armed spiral PCA modes, targets are governed by (parallel) alternating hot and cold rings.

We next consider the effect of the wall heat transfer coefficient by varying Bi_p for R/d_p = 10 and Da = 0.195. Based on the literature data, we fixed the range for Bi_p as (0, 1.2), with 0 corresponding to adiabatic conditions.[51,52] Symmetry breaking rotating and target patterns emerge from Hopf bifurcation at $Bi_p \approx 0.036$ (Figure 5a). Similar to the presence of a

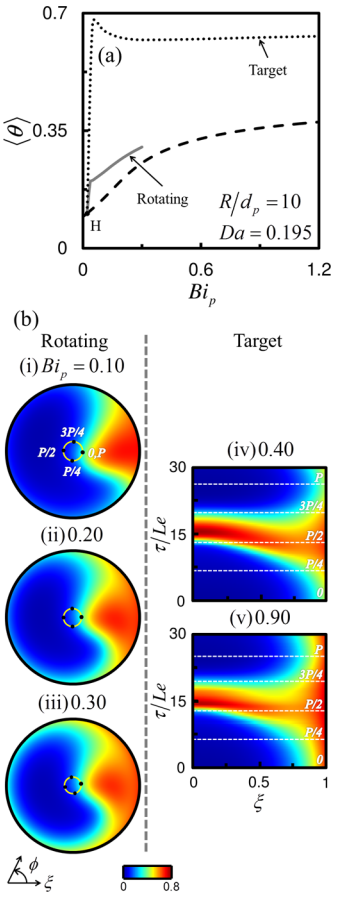

Figure 5. (a) Global bifurcation diagram showing the dependence of exit temperature $\langle\theta\rangle$ on Bi_p for 1-D base steady states (solid black, stable; dashed black, unstable), rotating (solid gray), and target (dotted) patterns. H indicates Hopf bifurcation point. (b) Snapshots of transversal temperature depicting rotating (i–iii) and target (iv–v) patterns for different Bi_p.

threshold R/d_p for coexistence of rotating and target patterns, we find there exists a threshold Bi_p beyond which only target patterns are found. While the dynamics of the rotating patterns for different Bi_p are presented in Figure 5b-i–iii, those for targets are in Figure 5b-iv,v. The amplitude $\mathcal{A}_p$ and period of oscillations P for typical values of Bi_p are presented in Table 2.

Table 2. Amplitude $\mathcal{A}_p$ and Period of Oscillation P for Different Bi_p for the Rotating and Target Patterns in Figure 5[a]

	Bi_p				
	0.1	0.2	0.3	0.4	0.9
	Rotating Pattern				
$\mathcal{A}_p$	0.0058	0.0055	0.0051		
P	28.61	24.72	23.66		
	Target Pattern				
$\mathcal{A}_p$	0.6010	0.5489	0.5103	0.4751	0.3906
P	32.84	27.89	26.48	26.13	25.60

[a] Da = 0.195, R/d_p = 10, and all other parameters as in eq 19.

DOI: 10.1021/acs.iecr.5b01048
Ind. Eng. Chem. Res. XXXX, XXX, XXX–XXX

The motion of the tip (for rotating patterns) is captured by a circle (yellow), and the tip location at four different times in one time period (P) is marked by black dots on the circle. PCA modes of the rotating and target patterns (in Figure 5b) are presented in Figure S3 in the Supporting Information. PCA suggests that higher modes containing two hot zones interspersed between two cold zones contributes appreciably (~10% for Bi_p = 0.10) to the overall dynamics. However, with increase in the Bi_p, the contribution from higher modes decrease and cause the rotating patterns branch to terminate. As a consequence, the reactor jumps to the target patterns branch.

Onset of Spiral Patterns. Given that for Bi_p = 0.25 and Da = 0.195 an increase in R/d_p forced the hot zone in the rotating patterns to curl, we next asked a question whether there are practical conditions where spiral patterns may exist. By conducting extensive dynamical simulations for various parameter values within the Hopf neutral stability curves (Figure 1a,b), we found that different types of spiral patterns exist very close to the Hopf bifurcation point, and we present in this section the formation and dynamics of these patterns.

We present the dynamics of the rich variety of rotating and spiral patterns obtained for Bi_p = 0.25 and Da = 0.175 for various R/d_p in the form of the locus of tip motion (yellow circle) with black dot representing the position of the tip at the start of the cycle, that is, τ/Le = 0 (Figure 6a). Note that the locus is superimposed on the spatial temperature profile of the pattern at τ/Le = 0. The period of oscillation P of the patterns

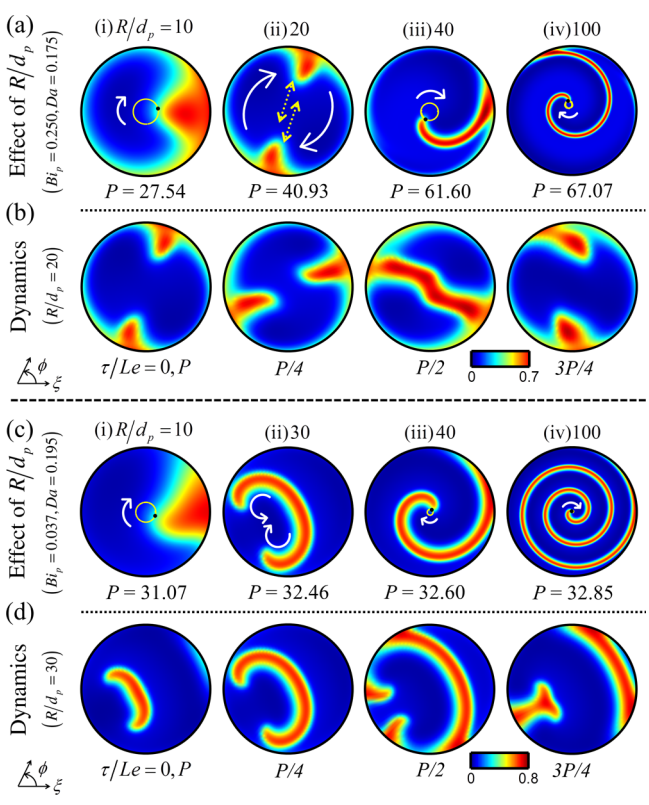

Figure 6. (a) Snapshot of spatiotemporal pattern at Da = 0.175, Bi_p = 0.25 for different R/d_p. (b) Spatiotemporal dynamics of two-hot zones rotating pattern at R/d_p = 20 (a-ii). (c) Snapshot of spatiotemporal pattern at Da = 0.195, Bi_p = 0.037 for different R/d_p. (d) Spatiotemporal dynamics of two-arm rotating pattern at R/d_p = 30 (c-ii).

in τ/Le is presented below each snapshot. A rotating pattern with one hot zone found at R/d_p = 10 is in Figure 6a-i. The nature of hot zone rotation R/d_p = 10 is similar to that in Figure 4b-i; henceforth, we refer to this as the simple rotating pattern. Increasing the reactor radius from 10 to 20 causes the hot zone in the simple rotating pattern to split into two hot zones at the outer rim with both rotating in the cross-section (Figure 6a-ii). As the pattern has two hot zones, two tips are expected. However, the tip identification approach in eq 20 fails to identify both tips as only one supremum of the cross-product was found. Therefore, we present the complex motion for this case in Figure 6b at different time points in one cycle. During one period of oscillation, both hot zones expanded, shrunk, merged, separated (indicated by yellow dashed arrows), and rotated clockwise (indicated by white solid arrows). While merging and expanding over a cycle, the hot zones also rotated in the cross-section by $\pi/3$ radians. Note that the expansion and shrinking of the hot zones caused the tip to move closer to and away from the wall. The two hot zones merged and separated, respectively, at $P/2$ (Figure 6b) near ξ = 0. [Note that similar dynamics was observed for R/d_p = 15 as well (data not shown).] When R/d_p is increased further to 40, the hot zones curled even further and formed a clockwise-rotating, inward-moving spiral pattern (Figure 6a-iii) whose tip motion is captured by the corresponding locus. With any further increase of R/d_p (up to 100), the clockwise-rotating, inward moving spirals were preserved (Figure 6a-iv) but with smaller diameter tip-circle. PCA modes for each of these cases are presented in Figure S4 in Supporting Information. Modes with intricate structures dominate the dynamics for R/d_p = 20. In the case of R/d_p = 40, the dynamics is equally dominated by multiple modes, each of which appears to permit two arms of alternating hot and cold regions, suggesting the onset of spirals. On the other hand, for R/d_p = 100, the dynamics is captured by multiple many-arm modes. The period of oscillations increases considerably with R/d_p, suggesting that the frequency of motion increases with a decrease in the domain size.

We next present the onset of spiral patterns near the Hopf bifurcation point for Bi_p = 0.037 and Da = 0.195 when the reactor radius is increased. For these set of parameters and R/d_p = 10, that is, mild heat transport with $Bi = Bi_p(R/d_p)$ = 0.37, a simple rotating pattern (similar to that in Figure 5b-i) was found (Figure 6c-i). The locus of the tip is presented as yellow circle. An increase in R/d_p to 30 (Bi = 1.11), that is, increase in the rate of wall heat transport, led to breakup of the pattern from the outer rim and, over one cycle, simultaneous expansion, curling, and movement of a band of hot zone across the reactor cross-section, as captured in the snapshots at different time points in one cycle of oscillation in Figure 6d. The hot zone started at a certain location in the reactor (Figure 6d-i) containing a band and two tips on either end of the band. Within a quarter period time, while the hot zone moved across the reactor, the ends of the hot zone curled in. Note that while the curling of one of the two tips of the hot zone occurred in a clockwise direction, the other tip curled anti-clockwise (Figure 6d-ii). Just after the middle of the cycle, that is, $\tau/Le = P/2$, the curling tip of the hot zones merged, and by the end of the cycle a band separated from the joined tips and exited from the diametrically opposite location of the cross-section (Figure 6d-iv). The leftover hot zone remains trapped in the reactor, and the cycle continues. [Note that this type of spatiotemporal motion is called anti-spirals.[53]] Upon further increasing R/d_p to 40, clockwise-rotating spirals were found (Figure 6c-iii), which

DOI: 10.1021/acs.iecr.5b01048
Ind. Eng. Chem. Res. XXXX, XXX, XXX−XXX

can be viewed as a combination of rotating hot zone and targets. In fact, further increase of R/d_p beyond 40 leads only to spirals but with multiple bands present simultaneously in the cross-section, indicating that these spirals arise by a combination of rotating pulse and multiple-ring targets (see Figure S5 in Supporting Information).

CONCLUSIONS AND DISCUSSION

Spatiotemporal pattern formation in packed-bed reactors has been predicted to occur under adiabatic conditions and is known to strongly depend on reaction kinetics.[31] Packed-bed reactors are usually operated under non-adiabatic conditions, and maintaining perfectly adiabatic conditions, even in laboratory-scale reactors, is extremely difficult. Using a blocking−reactivation kinetic model, which is well validated for ethylene hydrogenation processes, we predict formation of a rich variety of intricate patterns, such as rotating patterns, target patterns, spirals, and anti-spirals, in catalytic, shallow, packed-bed reactors under non-adiabatic conditions. These patterns are rather different from those predicted under adiabatic conditions. Prediction of hot zones in shallow reactors under non-adiabatic conditions is a step towards finding pattern formation in more realistic long, non-adiabatic reactors.

Identification of an appropriate initial guess using linear stability analysis is necessary for simulation of spatiotemporal patterns. Under non-adiabatic conditions, the coefficient of the linearized reaction term in the model equation will be an *a priori* unknown function of the radial position, making the linearized model equations *not* amenable to analytical solution strategies. We therefore propose a combination of analytical (in azimuthal direction) and numerical treatment to solve the eigenvalue problem in eq 14, and the solution is used to predict spatiotemporal patterns.

Our study shows that non-adiabatic reactors can permit inwardly moving spirals that can be obtained from rotating patterns and/or inwardly moving targets by perturbing the parameters. For example, for a reactor with R/d_p = 40 and certain wall heat flux (Bi_p = 0.25), a slight change in the residence time (Da) takes the reactor from a single ring target pattern (at Da = 0.195, Figure 4) to clockwise-rotating spiral patterns (at Da = 0.175, Figure 6a). This may be due to the fact that a slight perturbation of Da by 0.02 makes the system operate near the Hopf bifurcation (Figure 1b), where multi-arm modes (see Figure S4 in Supporting Information) may interact to force complex overall spatiotemporal dynamics. We found that, for R/d_p = 100, decreasing Bi_p forces targets (Figure 4b-vi) to become spirals (Figure 6c-iv). Moreover, increasing the reactor diameter, which is an important scale-up parameter, causes a transition from rotating patterns to spirals, where again higher modes seem to orchestrate the dynamics (Figure 6a,c). In fact, such a transition and interaction of higher modes contributing to the dynamics have been noted during NO + CO surface reaction on microstructured Pt(100).[54] Golubitsky et al.[47] suggested that such interactions dictate spirals and that non-zero wall flux is necessary for spiral patterns to form. This is due to the fact that zero wall flux cannot permit multi-arm spiral modes. Moreover, targets can be viewed as a superposition of clockwise- and anti-clockwise-rotating multi-arm spirals with same amplitudes.[47] This embedding of spirals in targets could be the cause for the observed transition between the two, under appropriate perturbations.

Our study also shows that rotating patterns may form in shallow, non-adiabatic packed-bed reactor for a wide range of reactor radius, R/d_p, even for small Bi_p = 0.037 (Figure 6c). The dominant modes that govern the rotating patterns (for sufficiently large reactor diameter) are similar to those obtained for traveling waves or band motion in adiabatic reactors.[30,31] This suggests that mild wall heat transfer (characterized by a small wall heat transfer coefficient) may force the traveling waves or band motion at Bi_p = 0 (adiabatic condition) to transition into rotating waves under non-adiabatic conditions.

Experimental studies conducted under atmospheric conditions in shallow, packed-bed reactors show that the frequency of rotating patterns is about 7×10^{-5} Hz during CO oxidation,[50] and the frequency of anti-phase motion is about 3×10^{-4} Hz during hydrogenation of ethylene and acetylene mixtures.[11] In our study, we found the frequency of oscillations to be in the range 2.45×10^{-5}−6.95×10^{-5} Hz for a typical reactor residence time of 2.7 s used in these laboratory experiments.[11] Hartmann et al.[54] noted that, during NO + CO surface reaction on microstructured Pt(100), the spiral pattern oscillation frequency was increased about 3 times by decreasing the domain size 2.5 times. Moreover, we found that the frequency increases with Bi_p (Table 2). Given that the extent of wall heat transport is characterized by the tunable parameter $Bi = Bi_p(R/d_p)$, and Bi_p and R/d_p have opposing effects on the oscillation frequency, we conjecture that there must be an optimal Bi at which a maximum frequency may exist. Knowledge of the maximum oscillation frequency can help design control strategies for good heat management.

Reactor scale-up is an important aspect in designing industrial-scale processes. We find that doubling the reactor diameter (from R/d_p = 10 to 20) causes the emergence of complex rotating patterns containing multiple interacting hot zones (Figure 6a). However, further doubling the reactor domain (R/d_p = 40) leads to the emergence of clockwise, inward-moving spiral patterns (Figure 6a). Tracking the tip motion is traditionally used to characterize rotating and spiral patterns.[55] However, when multiple hot zones rotate or spiral simultaneously, an objective, frame-invariant method (which can be automated) to track motion of all the tips is currently unavailable. Development of such a method could prove useful in characterizing complex spatiotemporal patterns containing multiple interacting hot zones, as is the case observed in our study when Bi_p = 0.25, Da = 0.175, R/d_p = 20 (Figure 6a-ii) or Bi_p = 0.037, Da = 0.195, R/d_p = 30 (Figure 6c-ii) and in other experimental studies.[11]

Strong interactions between characteristically different higher transversal modes govern complex spatiotemporal patterns. It is an open question as to what these interactions are, what different classes of patterns these interactions may lead to, and how these depend on various system parameters. A systematic method to identify the interactions between different transversal spatial modes is needed to address these questions.

APPENDIX I

Codimension-1 Locus

1. Construction of Hopf Neutral Stability Locus. Hopf neutral stability point is obtained by solving simultaneously eq 16 and the following:

$$[\mathbb{D}_{\boldsymbol{u}}\mathbb{F}|_{\boldsymbol{u}_{ss}} - \mathbb{P}]\cdot\boldsymbol{\omega}_r(\xi) + \sigma\boldsymbol{\omega}_i(\xi) = 0 \quad \text{(AI-1)}$$

$$[\mathbb{D}_{\boldsymbol{u}}\mathbb{F}|_{\boldsymbol{u}_{ss}} - \mathbb{P}]\cdot\boldsymbol{\omega}_i(\xi) - \sigma\boldsymbol{\omega}_r(\xi) = 0 \quad \text{(AI-2)}$$

$$\|\boldsymbol{\omega}_r(\xi)\| + \|\boldsymbol{\omega}_i(\xi)\| - 1 = 0 \quad \text{(AI-3)}$$

DOI: 10.1021/acs.iecr.5b01048
Ind. Eng. Chem. Res. XXXX, XXX, XXX−XXX

$$\boldsymbol{\omega}_r(\xi)\cdot\boldsymbol{\omega}_i(\xi) = 0 \quad \text{(AI-4)}$$

Note that eqs AI-1 and AI-2 are obtained by separating the real and complex parts of eq 17, and eqs AI-3 and AI-4 together ensure non-triviality. Hopf neutral stability curve is obtained by performing a pseudo-arc length continuation[46] of the Hopf neutral stability points.

2. Construction of Limit Point Locus. At a limit point, the eigenvalue λ is zero, and the corresponding eigenvector $\boldsymbol{\omega}(\xi)$ is purely real. Therefore, a limit point may be obtained by simultaneously solving eq 16 and $\mathbb{D}_u\mathbb{F}|_{u_{ss}}\cdot\boldsymbol{\omega}(\xi) = 0$ with the non-triviality condition $\|\boldsymbol{\omega}(\xi)\| = 1$. Codimension-1 limit point locus (in Figure 1a) is obtained by performing a pseudo-arc length continuation[46] of the limit point.

APPENDIX II

Principal Component Analysis

Spatiotemporal data $\boldsymbol{u}(\xi,\phi,\tau)$ are represented by a series $\boldsymbol{u}(\xi,\phi,\tau) = \sum_{i=1}^{n}\mathcal{A}_i(\tau)\mathrm{M}_i(\xi,\phi)$, where $\mathcal{A}_i(\tau)$ and $\mathrm{M}_i(\xi, \phi)$ respectively represent the orthogonal time-dependent amplitudes and time-independent spatial modes or PCA modes.[29] Therefore,

$$\langle \mathrm{M}_i(\xi, \phi)\cdot\mathrm{M}_j(\xi, \phi)\rangle = \delta_{ij} \quad \text{(AII-1)}$$

$$\overline{\mathcal{A}_i(\tau)\mathcal{A}_j(\tau)} = \lambda_i\delta_{ij} \quad \text{(AII-2)}$$

Using q snapshots of the temporal pattern, PCA modes $\mathrm{M}_i(\xi,\phi)$ are estimated by finding the eigenvectors of the eigenvalue problem

$$\mathbb{A}\mathrm{M}_i(\xi, \phi) = \lambda_i\mathrm{M}_i(\xi, \phi) \quad \text{(AII-3)}$$

where the autocorrelation matrix $\mathbb{A} = (1/q)\sum_{i=1}^{q}\boldsymbol{u}(\xi,\phi,\tau_i)\boldsymbol{u}[(\xi,\phi)',\tau_i]$ and λ_i captures the energy corresponding to PCA mode $\mathrm{M}_i(\xi,\phi)$, that is, the fractional contribution of the PCA mode to the overall dynamics of the pattern. The amplitudes $\mathcal{A}_i(\tau)$ are obtained using the expression

$$\mathcal{A}_i(\tau) = \sum_{i=1}^{q}\boldsymbol{u}(\xi, \phi, \tau_i)\mathrm{M}_i(\xi, \phi) \quad \text{(AII-4)}$$

which is essentially a projection of the data set on the PCA modes. The PCA routine in Matlab was used to identify the PCA modes and the amplitudes.

ASSOCIATED CONTENT

Supporting Information

Figure S1: Time series of exit temperature $\langle\theta\rangle$, exit concentration $\langle x\rangle$, and fraction of blocked catalytically active sites $\langle\Theta\rangle$ for rotating pattern at $Da = 0.195$, $Bi_p = 0.25$, $R/d_p = 10$. Figures S2−S5: Principal component analyses of spatiotemporal pattern presented in Figures 4b, 5b, and 6a,c. The Supporting Information is available free of charge on the ACS Publications website at DOI: 10.1021/acs.iecr.5b01048.

AUTHOR INFORMATION

Corresponding Author

*Tel.: +91-22-2576-7222. E-mail: ganeshav@iitb.ac.in.

Author Contributions

K.N. and G.A.V. conceived and designed the study, K.N. performed the study, and K.N. and G.A.V. analyzed the results and wrote the manuscript. Both authors have given approval to the final version of the manuscript.

Notes

The authors declare no competing financial interest.

ACKNOWLEDGMENTS

We thank the CDAC for providing access to the high-performance computing facility. We are thankful to Prabhu Ramachandran, Rochish Thaokar, and Mahesh Tirumkudulu for many helpful discussions and advice.

ABBREVIATIONS

A_c = constant coefficient for initial condition in eq 18
$\mathcal{A}$ = orthogonal time-dependent amplitude
$\mathcal{A}_p$ = amplitude of oscillation of exit temperature
$\mathbb{A}$ = autocorrelation matrix
Bi = Biot number
$\mathbb{B}_1$ = dimensionless rate of blocking of catalytic active sites, defined by eq 3
$\mathbb{B}_2$ = dimensionless rate of reactivation of blocked sites, defined by eq 3
C = concentration, mol m^{-3}
C_p = specific heat capacity, J kg^{-1} K^{-1}
d_p = particle diameter, m
D = species diffusion coefficient, m^2 s^{-1}
Da = Damköhler number, defined by eq 8
$\mathbb{D}_u\mathbb{F}$ = first Fréchet derivative
E = activation energy, J mol^{-1}
$\mathbb{F}$ = vector of steady-state equations
h = wall heat transfer coefficient, W m^{-2} K^{-1}
H = Hopf point
k = reaction rate constant, s^{-1}
k^0 = Arrhenius rate constant, s^{-1}
L = reactor length, m
Le = Lewis number
$\mathbf{M}$ = orthogonal matrix
N = radial grid points
P = period of oscillation
Pe = Peclet number
$\mathbb{P}$ = perturbation
q = number of snapshots of the temporal pattern
r = radial coordinate, m
R = radius of the reactor, m
$\bar{R}$ = universal gas constant, J mol^{-1} K^{-1}
$\mathbb{R}$ = dimensionless reaction rate, defined by eq 9
t = time, s
T = temperautre, K
$\boldsymbol{u}$ = vector of state variables
v = superficial velocity, m s^{-1}
x = conversion
z = axial coordinate, m

Greek Letters

Θ = fraction of blocked catalytic active sites in eq 2
τ = dimensionless time, defined by eq 4
θ = dimensionless temperature
β = adiabatic temperature rise, defined by eq 8
η = dimensionless axial coordinate, defined by eq 8
ξ = dimensionless radial coordinate, defined by eq 8
γ = dimensionless activation energy, defined by eq 8
$-\Delta H$ = heat of the reaction, J mol^{-1}
ε = bed voidage
λ = eigenvalue
$\bar{\lambda}$ = effective thermal conductivity, Wm^{-1} K^{-1}
ϕ = azimuthal coordinate

DOI: 10.1021/acs.iecr.5b01048
Ind. Eng. Chem. Res. XXXX, XXX, XXX−XXX

σ = coefficient of imaginary eigenvalue
$\boldsymbol{\omega}$ = eigenvector
∇ = gradient operator

Others

$\cdot$ = dot product
$\times$ = cross product
$\langle ... \rangle$ = average quantity
$\|\cdot\|$ = 2-norm
$\nabla_{\perp}^{2}$ = Laplacian in polar coordinates
sup = supremum

Superscripts

h = heat
m = mass
t = transpose

Subscripts

BL = blocking
RE = reactivation
in = inlet
s = solid
f = fluid
a = axial
$\perp$ = transversal
p = particle
w = wall
ss = steady state
m = azimuthal mode number
r = real
i = imaginary

REFERENCES

(1) Boreskov, G. K.; Matros, Y. S.; Klenov, O. P.; Lugovskoi, V. I.; Lakhmostov, V. S. Local nonuniformities in a catalyst bed. *Dokl. Akad. Nauk SSSR* **1981**, *258*, 1418.

(2) Matros, Y. S. *Unsteady Processes in Catalytic Reactors*; Elsevier: Amsterdam, 1985.

(3) Barkelew, C. H.; Gambhir, B. S. Stability of trickle-bed reactors. *ACS Symp. Ser.* **1984**, *237*, 61−81.

(4) Wicke, E.; Onken, H. U. Periodicity and chaos in a catalytic packed bed reactor for CO oxidation. *Chem. Eng. Sci.* **1988**, *43*, 2289−2294.

(5) Wicke, E.; Onken, H. U. Bifurcation, periodicity and chaos by thermal effects in heterogeneous catalysis. In *From Chemical to Biological Organization*; Markus, M., Muller, S. C., Nicolis, G., Eds.; Springer-Verlag: Berlin/New York, 1988; pp 68−81.

(6) Marwaha, B.; Annamalai, J.; Luss, D. Hot zone formation during carbon monoxide oxidation in a radial flow reactor. *Chem. Eng. Sci.* **2001**, *56*, 89−96.

(7) Marwaha, B.; Luss, D. Formation and dynamics of a hot zone in radial flow reactor. *AIChE J.* **2002**, *48*, 617−624.

(8) Digilov, R. M.; Nekhamkina, O.; Sheintuch, M. Catalytic spatiotemporal thermal patterns during CO oxidation on cylindrical surfaces: Experiments and simulations. *J. Chem. Phys.* **2006**, *124*, 034709.

(9) Marwaha, B.; Luss, D. Hot zones formation in packed bed reactors. *Chem. Eng. Sci.* **2003**, *58*, 733−738.

(10) Marwaha, B.; Sundarram, S.; Luss, D. Dynamics of hot zones on top of packed-bed reactors. *Chem. Eng. Sci.* **2004**, *59*, 5569−5574.

(11) Pinkerton, B.; Luss, D. Hot zone formation during hydrogenation of ethylene and acetylene mixtures in a shallow packed bed reactor. *Ind. Eng. Chem. Res.* **2007**, *46*, 1898−1903.

(12) Digilov, R.; Nekhamkina, O.; Sheintuch, M. Thermal imaging of breathing patterns during CO oxidation on a Pd/glass cloth. *AIChE J.* **2004**, *50*, 163−172.

(13) Kimmerle, B.; Baiker, A.; Grunwaldt, J. D. Oscillatory behaviour of catalytic properties, structure and temperature during the catalytic partial oxidation of methane on Pd/Al_2O_3. *Phys. Chem. Chem. Phys.* **2010**, *12*, 2288−2291.

(14) Viswanathan, G. A.; Sheintuch, M.; Luss, D. Transversal hot zones formation in catalytic packed-bed reactors. *Ind. Eng. Chem. Res.* **2008**, *47*, 7509−7523.

(15) Gundlapally, S. R.; Agrawal, R.; West, D. H.; Balakotaiah, V. Influence of non-uniform activity and conductivity on stationary and moving patterns in catalytic reactors. *Chem. Eng. Sci.* **2010**, *65*, 1522−1538.

(16) Jaffe, S. B. Hot spot simulation in commercial hydrogenation processes. *Ind. Eng. Chem. Process Des. Dev.* **1976**, *15*, 410−416.

(17) Agrawal, R.; West, D. H.; Balakotaiah, V. Modeling and analysis of local hot spot formation in down-flow adiabatic packed-bed reactors. *Chem. Eng. Sci.* **2007**, *62*, 4926−4943.

(18) Subramanian, S.; Balakotaiah, V. Analysis and classification of reaction-driven stationary convective patterns in a porous medium. *Phys. Fluids* **1997**, *9*, 1674−1695.

(19) Benneker, A. H.; Kronberg, A. E.; Westerterp, K. R. Influence of buoyancy forces on the flow of gases through packed beds at elevated pressures. *AIChE J.* **1998**, *44*, 263−270.

(20) Sundarram, S.; Marwaha, B.; Luss, D. Global-coupling induced temperature patterns on top of packed-bed reactors. *Chem. Eng. Sci.* **2005**, *60*, 6803−6805.

(21) Nekhamkina, O.; Digilov, R.; Sheintuch, M. Modeling of temporally complex breathing patterns during Pd-catalyzed CO oxidation. *J. Chem. Phys.* **2003**, *119*, 2322−2332.

(22) Schmitz, R. A.; Tsotsis, T. T. Spatially patterned states in systems of interacting catalyst particles. *Chem. Eng. Sci.* **1983**, *38*, 1431−1437.

(23) Balakotaiah, V.; Christoforatou, E. L.; West, D. H. Transverse concentration and temperature nonuniformities in adiabatic packed-bed catalytic reactors. *Chem. Eng. Sci.* **1999**, *54*, 1725−1734.

(24) Yakhnin, V.; Menzinger, M. On transverse patterns in packed-bed catalytic reactors. *Chem. Eng. Sci.* **2001**, *56*, 2233−2236.

(25) Poling, B. E.; Prausnitz, J. M.; O'Connell, J. P. *The properties of gases and liquids*, 5th ed.; McGraw-Hill: New York, 2000.

(26) Elsari, M.; Hughes, R. Axial effective conductivities of packed beds. *Appl. Therm. Eng.* **2002**, *22*, 1969−1980.

(27) Viswanathan, G.; Luss, D.; Bindal, A.; Khinast, J. Stationary transversal hot zones in adiabatic packed-bed reactors. *AIChE J.* **2005**, *51*, 3028−3038.

(28) Viswanathan, G. A.; Luss, D. Model prediction of hot spots formation in shallow adiabatic packed-bed reactors. *AIChE J.* **2006**, *52*, 1533−1538.

(29) Viswanathan, G. A.; Luss, D. Moving transversal hot zones in adiabatic, shallow packed-bed reactors. *AIChE J.* **2006**, *52*, 705−717.

(30) Sundarram, S.; Viswanathan, G. A.; Luss, D. Reactor diameter impact on hot zone dynamics in an adiabatic packed bed reactor. *AIChE J.* **2007**, *53*, 1578−1590.

(31) Viswanathan, G. A.; Luss, D. Hot zones formation and dynamics in long adiabatic packed-bed reactors. *Ind. Eng. Chem. Res.* **2006**, *45*, 7057−7066.

(32) Nekhamkina, O.; Sheintuch, M. Transversal patterns in three-dimensional packed bed reactors: Oscillatory kinetics. *AIChE J.* **2010**, *56*, 2887−2897.

(33) Imbihl, R.; Ertl, G. Oscillatory kinetics in heterogeneous catalysis. *Chem. Rev.* **1995**, *95*, 697−733.

(34) Wicke, E.; Kummann, P.; Keil, W.; Schiefler, J. Unstable and oscillatory behavior in heterogeneous catalysis. *Phys. Chem. Chem. Phys.* **1980**, *84*, 315−323.

(35) Bartholomew, C. H.; Farrauto, R. J. *Fundamentals of Industrial Catalytic Processes*, 2nd ed.; Wiley: New York, 2006.

(36) Nekhamkina, O.; Sheintuch, M. Are 3-D models necessary to simulate packed bed reactors? Analysis and 3-D simulations of adiabatic and cooled reactors. *AIChE J.* **2012**, *58*, 3494−3503.

(37) Bos, A. N. R.; Hof, E.; Kuper, W.; Westerterp, K. R. The behavior of a single catalyst pellet for the selective hydrogenation of ethyne in ethene. *Chem. Eng. Sci.* **1993**, *48*, 1959−1969.

DOI: 10.1021/acs.iecr.5b01048
Ind. Eng. Chem. Res. XXXX, XXX, XXX−XXX

(38) Golubitsky, M.; Schaeffer, D. *Singularities and groups in bifurcation theory*; Springer-Verlag: New York, 1984; Vol. *1*.
(39) Chakraborty, S.; Balakotaiah, V. Low-dimensional models for describing mixing effects in laminar flow tubular reactors. *Chem. Eng. Sci.* **2002**, *57*, 2545−2564.
(40) Viswanathan, G. A. Transversal temperature patterns in packed-bed reactors. Ph.D. Dissertation, University of Houston, Houston, TX, 2004.
(41) Balakotaiah, V.; Gupta, N.; West, D. H. Transport limited pattern formation in catalytic monoliths. *Chem. Eng. Sci.* **2002**, *57*, 435−448.
(42) Middya, U.; Luss, D. Impact of global interaction on pattern-formation on a disk. *J. Chem. Phys.* **1995**, *102*, 5029−5036.
(43) Deuflhard, P.; Hairer, E.; Zugck, J. One-step and extrapolation methods for differential-algebraic systems. *Numer. Math.* **1987**, *51*, 501−516.
(44) Ehrig, R.; Nowak, U.; Oeverdieck, L.; Deuflhard, P. Advanced extrapolation methods for large scale differential algebraic problems. In *High Performance Scientific and Engineering Computing*; Bungartz, H.-J., Durst, F., Zenger, C., Eds.; Springer: Berlin/Heidelberg, 1999; Vol. *8*, pp 233−241.
(45) Heroux, M. A.; Bartlett, R. A.; Howle, V. E.; Hoekstra, R. J.; Hu, J. J.; Kolda, T. G.; Lehoucq, R. B.; Long, K. R.; Pawlowski, R. P.; Phipps, E. T. An overview of the Trilinos project. *ACM Trans. Math. Softw.* **2005**, *31*, 397−423.
(46) Salinger, A. G.; Burroughs, E. A.; Pawlowski, R. P.; Phipps, E. T.; Romero, L. A. Bifurcation tracking algorithms and software for large scale applications. *Int. J. Bifurcation Chaos Appl. Sci. Eng.* **2005**, *15*, 1015−1032.
(47) Golubitsky, M.; Knobloch, E.; Stewart, I. Target patterns and spirals in planar reaction-diffusion dystems. *J. Nonlinear Sci.* **2000**, *10*, 333−354.
(48) Palacios, A.; Gunaratne, G. H.; Gorman, M.; Robbins, K. A. Karhunen-Loève analysis of spatiotemporal flame patterns. *Phys. Rev. E: Stat. Phys., Plasmas, Fluids, Relat. Interdiscip. Top.* **1998**, *57*, 5958−5971.
(49) Graham, M. D.; Lane, S. L.; Luss, D. Proper orthogonal decomposition analysis of spatiotemporal temperature patterns. *J. Phys. Chem.* **1993**, *97*, 889−894.
(50) Marwaha, B.; Sundarram, S.; Luss, D. Dynamics of transversal hot zones in shallow packed-bed reactors. *J. Phys. Chem. B* **2004**, *108*, 14470−14476.
(51) Dixon, A. G. Wall and particle-shape effects on heat-transfer in packed-beds. *Chem. Eng. Commun.* **1988**, *71*, 217−237.
(52) Henda, R.; Machac, A.; Nilsson, B. Heat and mass transport in a nonlinear fixed-bed catalytic reactor: Hot spots and thermal runaway. *Chem. Eng. J.* **2008**, *143*, 195−200.
(53) Vanag, V. K.; Epstein, I. R. Inwardly rotating spiral waves in a reaction-diffusion system. *Science* **2001**, *294*, 835−837.
(54) Hartmann, N.; Bär, M.; Kevrekidis, I. G.; Krischer, K.; Imbihl, R. Rotating chemical waves in small circular domains. *Phys. Rev. Lett.* **1996**, *76*, 1384−1387.
(55) Steinbock, O.; Zykov, V.; Muller, S. C. Control of spiral-wave dynamics in active media by periodic modulation of excitability. *Nature* **1993**, *366*, 322−324.

DOI: 10.1021/acs.iecr.5b01048
Ind. Eng. Chem. Res. XXXX, XXX, XXX−XXX